metals

MDPI

Article

Response of the Metastable Pitting Corrosion of Laser Powder Bed Fusion Produced Ti–6Al–4V to H^+ Concentration Changes

Yuwei Cui [1], Liangyu Chen [1,*], Liqiang Wang [2], Jun Cheng [3] and Laichang Zhang [4,*]

[1] School of Materials Science and Engineering, Jiangsu University of Science and Technology, Zhenjiang 212100, China
[2] State Key Laboratory of Metal Matrix Composites, School of Material Science and Engineering, Shanghai Jiao Tong University, No. 800 Dongchuan Road, Shanghai 200240, China
[3] Shaanxi Key Laboratory of Biomedical Metal Materials, Northwest Institute for Nonferrous Metal Research, Xi'an 710016, China
[4] School of Engineering, Edith Cowan University, 270 Joondalup Drive, Joondalup, Perth, WA 6027, Australia
* Correspondence: lychen@just.edu.cn (L.C.); lczhangimr@gmail.com or l.zhang@ecu.edu.au (L.Z.)

Abstract: There is limited research on metastable pitting corrosion in an acidic environment, and acid is a major challenge for material corrosion. Therefore, this work investigated the metastable pitting corrosion of laser powder bed fusion (LPBF)-produced Ti–6Al–4V, in Hank's solution, at different pH values (pH = 3, 5, and 7). This work investigated the effect of acid on the characteristics of passive films, as well as the change in metastable pitting behavior. Based on the results of electrochemical impedance spectroscopy (EIS) and X-ray photoelectron spectroscopy (XPS), the passive film will be inhibited and dissolved under the influence of H^+. The higher the concentration of H^+, the thinner the passive film. Potentiodynamic polarization tests reveal that LPBFed Ti–6Al–4V in Hank's solution, at pH 3, has more obvious metastable pitting corrosion. This is because the higher the H^+ concentration, the more Cl^- is adsorbed on the surface of the passive film, which is prone to generate soluble chlorides by competitive adsorption with oxygen atoms and thus develop into metastable pitting corrosion.

Keywords: laser powder bed fusion; Ti–6Al–4V; metastable pitting corrosion; passive film; competitive adsorption

Citation: Cui, Y.; Chen, L.; Wang, L.; Cheng, J.; Zhang, L. Response of the Metastable Pitting Corrosion of Laser Powder Bed Fusion Produced Ti–6Al–4V to H^+ Concentration Changes. *Metals* **2023**, *13*, 514. https://doi.org/10.3390/met13030514

Academic Editors: Amir Mostafaei and Aleksander Lisiecki

Received: 29 December 2022
Revised: 16 February 2023
Accepted: 27 February 2023
Published: 3 March 2023

1. Introduction

Pitting corrosion exists in various fields, and frequently occurs on the surface of easily passivated metals [1–3]. As a complex corrosion process, pitting corrosion is influenced by many factors, including temperature, aggressive ions, applied potential, and so on [1,4]. Many years have passed since relative pitting corrosion research began, with a large portion of this research focusing on the characteristics of the passive film and metastable pitting corrosion (the transition state before stable pitting corrosion) [4–7]. The passive film, as a protective layer, and the initiation site of pitting corrosion on the metal surface, need to be understood to work out the corresponding mechanism response to pitting corrosion. Three principal mechanisms around the passive film response to pit initiation have been categorized: the breakdown mechanism of the passive film, the penetration mechanism of the passive film, and the adsorption mechanism [8–10]. Metastable pitting corrosion is regarded as the next stage of pit initiation, which determines the formation of stable pitting corrosion. The passive film has the potential to repair itself during pit nucleation, while if metastable pitting corrosion develops fast, stable pitting is still unavoidable. Metastable means unstable, and indicates the possibility of inhibiting the formation of the pit by elucidating the mechanics of metastable pitting corrosion.

Previously, our work has studied related research on metastable pitting [6]. That work found that the semiconductive property of the passive film has a relationship with

the migration of oxygen vacancies. According to MacDonald's point defect model (PDM) and the penetration mechanism of the passive film, the adsorption of aggressive ions (such as F^-, Br^-, Cl^-, etc.) from the outside of the film and a large number of oxygen vacancies result in the formation of numerous cation vacancies [6,11]. The excess cation vacancies condense into a void, namely, a pit. A lot of researchers have also reported similar results before, e.g., Refs. [12–14]. However, under certain conditions, such as acidic conditions, the aggressive Cl^- ions can squeeze out and occupy oxygen atoms in the passive film. Meanwhile, the metal surface forms a salt film, which is dissolved in solution and accelerates the metal corrosion. In addition, Qu et al. [15] demonstrated that titanium is prone to forming a chelate compound ($[Ti(OH)_3]L$) in artificial saliva, with lactic acid, which accelerated passive film dissolution and increased the tendency of pitting corrosion. They proposed that the addition of lactic acid changed the corrosion mechanism and accelerated the pitting corrosion [15]. Therefore, the passive film reacted with H^+ in an acidic environment, then tended to dissolve. As such, the metal surface was transformed from a passive state to an active state. At the moment, the presence of aggressive ions such as Cl^- would corrode a single point, resulting in localized corrosion. However, only a few studies have been conducted on the pitting corrosion behavior of metals in acid solutions, let alone metastable pitting corrosion. In addition, interestingly Cl^- exerts its aggressiveness more strongly in acidic environments, compared to other environments. Therefore, the focus of this work will be on this area.

Combined with our previous work, we decided to continue to adopt laser powder bed fusion (LPBF)-produced Ti–6Al–4V as a research object [6]. Ti–6Al–4V is currently a popular metal material for human implants, due to its excellent mechanical properties, corrosion resistance, and biocompatibility. The traditional manufacturing of the titanium alloy is gradually being abandoned, because the process is limited by the shape of the target part and the accuracy is low. More recently, a novel additive manufacturing technology, commonly known as 3D printing, has attracted a lot of attention. LPBF is one such additive manufacturing technology. The preparation process of LPBFed Ti–6Al–4V is different from its traditional preparation, it has a short cycle, high utilization, and is not limited by shape [16–18]. Furthermore, these advantages also determine many application scenarios for LPBFed Ti–6Al–4V, which indicates that LPBFed Ti–6Al–4V most likely needs to be applied in acidic environments. Moreover, pitting corrosion has been found in LPBFed Ti–6Al–4V used in many applications, which limits its future development [1,6,8,10,19–21].

As a result, this work studied the metastable pitting corrosion behavior of LPBFed Ti–6Al–4V in an acidic environment. The acidic environment was provided by Hank's solution, with lactic acid, and three different pHs were used (pH = 3, 5, and 7). The corresponding metastable pitting corrosion of LPBFed Ti–6Al–4V in solution with various pHs is discussed.

2. Experimental

2.1. Preparation of Samples and Solutions

Each LPBFed Ti–6Al–4V block for the experiments was 1 cm × 1 cm × 1 cm, and manufactured by an MTT SLM 250 HL machine. The whole preparation process was conducted under a high-purity protective gas (Ar) and a vacuum of 10^{-3} mbar. The equipment parameters were 1000 mm/s scan speed, 200 W laser power, and a 40 μm light spot. Simultaneously, the section line spacing was set at 100 μm, the layer thickness at 50 μm, and the "zigzag" mode was used for both scans. Electrochemical experiments require a high level of purity of the material surface, so some surface treatments were needed. First, a perforation was made in the blocks to facilitate the fixing of copper wires, then the gap between the copper wires and blocks was welded with solder to ensure good conductivity. Next, the entire block was sealed with epoxy resin, and only one 1 × 1 cm^2 surface was left for subsequent treatment. The retained surface was ground with SiC papers, from 400 to 2000 grit, and polished to a mirror finish with 1 μm diamond grinding paste. Then the samples were ultrasonically cleaned in alcohol, blown dry, and stored in

a dry box for use during the experiment. The samples in the subsequent electrochemical experiments all required the same surface treatment as above.

The acid environment was provided by Hank's solution with the addition of lactic acid. Hank's solution is produced by Hank's balanced salts (Heart Biological Technology Co., LTD., Beijing, China) with the addition of 0.35 g/L $NaHCO_3$, and the main compositions of Hank's salt are: 0.140 g/L $CaCl_2$, 0.4 g/L KCl, 0.06 g/L KH_2PO_4, 0.098 g/L $MgSO_4$, 8 g/L NaCl, 1 g/L $C_6H_{12}O_6$, 0.048 g/L Na_2HPO_4, and 0.011 g/L $C_{19}H_{14}O_5SNa$. The pH values of Hank's solution adjusted with lactic acid are 3, 5, and 7, respectively, as a way to control the change in H^+ concentration. Furthermore, during electrochemical experiments, Hank's solutions must be kept at 37 ± 0.5 °C.

2.2. Morphological Characterization

The morphology of LPBFed Ti–6Al–4V in Hnk's solutions at pH 3 was inspected using a scanning electron microscope (SEM). The model of the SEM device is Sigma HD, Zeiss, which was employed to characterize the pits on the sample surface after 1.0 V_{SCE} potentiostatic polarization.

2.3. X-ray Photoelectron Spectroscopy Characterization

The chemical compositions of the passive film formed on the samples were analyzed by X-ray photoelectron spectroscopy (XPS, ESCALAB 250XI, ESCALAB 250Xi T, ThermoFisher Scientific, Waltham, MA, USA). Samples were conducted 2500 s in Hank's solutions with different pH (pH = 3, 5, 7) under 1.0 VSCE potential. The test parameters for XPS are 500 μm spot diameter; the etching speed of 0.2 nm/s with argon ions. Using Al Kα X-rays as a light source (*hv* = 1486.6 eV) at 15 kV and 10 mA. Thermo Avantage 5.992 software was used to fit the XPS spectra.

2.4. Electrochemical Measurements

In this work, an electrochemical workstation (CHI660E, Shanghai Chenhua Company) equipped with a three-electrode system was used to examine the electrochemical tests. In this system, the working electrode (WE) was the sample, LPBFed Ti–6Al–4V; the counter electrode (CE) was a platinum sheet; and the reference electrode (RE) was a saturated calomel electrode. First of all, the cathodic polarization was conducted for three minutes, to ensure the passive film formed on the surface of samples in air had been removed completely (the current does not change with time in cathodic polarization tests). A potentiodynamic polarization test was performed, at a sweep rate of 0.2 mV/s, with a sweeping range of −0.25–2.0 V_{SCE}. Afterward, the open circuit potential (OCP) was measured for 1800 s, to make sure a stable passive film had formed on the sample surface. Potentiostatic polarization (PP) was performed after OCP, and conducted for 2500 s under 0.6, 0.7, 0.8, 0.9, and 1.0 V_{SCE} potentials. Then, the electrochemical impedance spectroscopy (EIS) was tested, which scanned samples in the range of 10^5 Hz to 10^{-2} Hz, with an AC amplitude of 10 mv. The EIS results were fitted with the ZView software. Moreover, the Mott–Schottky tests can be measured directly after EIS, and performed from the film-formation potential (0.6, 0.7, 0.8, 0.9, and 1.0 V_{SCE}) to −1.0 V_{SCE} under a 1 kHz frequency. The scan speed of the Mott–Schottky test was 10 mV/s. It should be noted that the entire experiments needed to be repeated at least three times under the same conditions.

3. Results

3.1. Morphological Features

Figure 1 exhibits the SEM images of the surface of the sample before and after pitting corrosion. The surface of LPBFed Ti–6Al–4V is smooth and flat, as shown in Figure 1a, which indicates an original surface without corrosion. In contrast, Figure 1b shows a pitting morphology of LPBFed Ti–6Al–4V in Hank's solution, at pH 3, after PP. The pit has been marked with a white dashed circle. Furthermore, the picture shows an irreversible steady-state pitting corrosion.

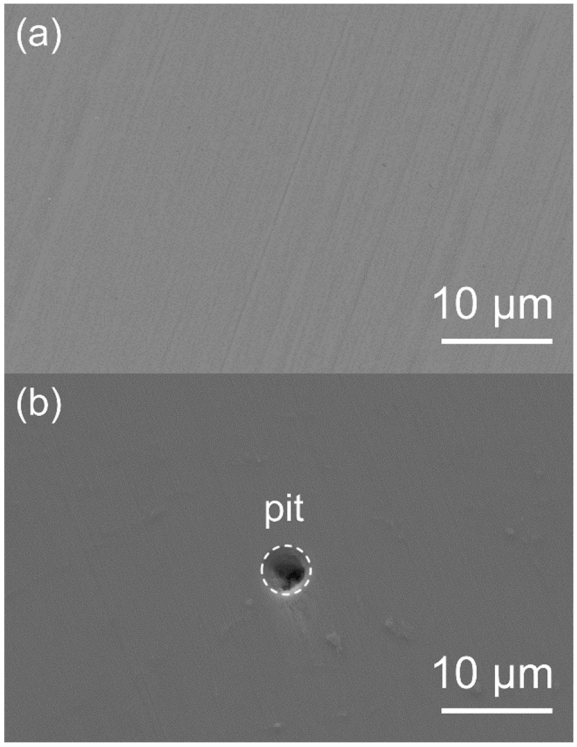

Figure 1. SEM pictures of the morphologies of LPBFed Ti–6Al–4V in Hank's solution, at pH 3, after PP: (**a**) the surface without corrosion and (**b**) one pit was discovered on the surface of the sample.

3.2. Potentiodynamic Polarization Test

Figure 2 exhibits the potentiodynamic polarization (PD) curves of LPBFed Ti–6Al–4V in Hank's solution, with different pH values (pH = 3, 5, and 7). During the whole PD process, three samples, with different pH values, show overlapped curves. At the same time, Table 1 lists the fitting results of the PD curves, including corrosion current density (I_{corr}), corrosion potential (E_{corr}), and corrosion rate. According to Faraday's law, the corrosion rate is calculated as follows [6]:

$$\text{Corrosion rate} = \frac{MI_{corr}}{nF\rho_m} \quad (1)$$

where M is the molar mass of Ti, which is equal to 47.87 g·mol^{-1} [17], n is the charge of the Ti ion, F is the Faraday constant, which is equal to 96,487 C mol^{-1} [17], and ρ_m is the density of the Ti–6Al–4V alloy, which is 4.43 g cm^{-3} [6]. The values of I_{corr} can be obtained by fitting the PD curves. According to the calculations, the corrosion rates for Ti–6Al–4V under pH 3, pH 5, and pH 7 were 0.2699×10^{-5} mm·y^{-1}, 0.1769×10^{-5} mm·y^{-1}, and 0.0935×10^{-5} mm·y^{-1}, respectively. The I_{corr} and E_{corr} showed opposite tendencies with decreasing pH values, with I_{corr} increasing, and E_{corr} decreasing. This indicates that the decreasing pH values directly influenced E_{corr} and facilitated alloy corrosion. It can be concluded that LPBFed Ti–6Al–4V is more susceptible to corrosion in Hank's solution at pH 3. Furthermore, current transition phenomena were observed in the inset of Figure 2. It is indicated that the passive film is in an unstable state above 1.0 V_{SCE} and prone to pit nucleation on the surface, and the whole phenomenon becomes more pronounced as the pH value decreases. Therefore, the corrosion resistance of LPBFed Ti–6Al–4V has a high potential to lead to metastable pitting corrosion, in addition to declining with lower pH values.

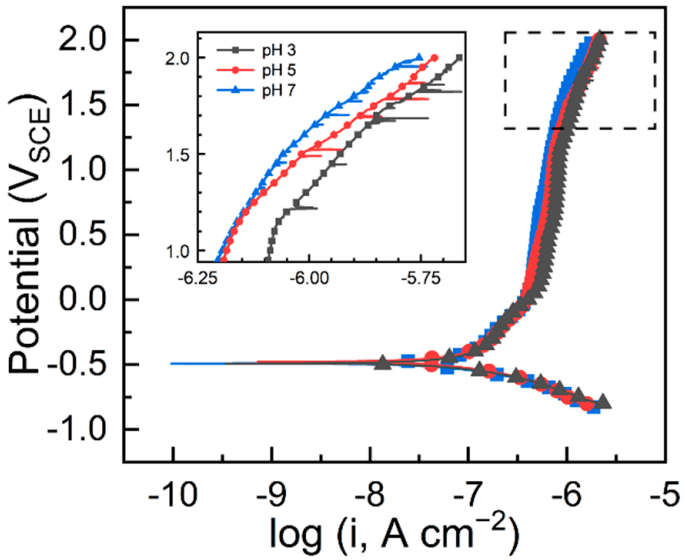

Figure 2. Potentiodynamic polarization curves of LPBFed Ti–6Al–4V in Hank's solution with different pH values, at 37 °C.

Table 1. Fitting results and calculated corrosion rate of potentiodynamic polarization curves of LPBFed Ti–6Al–4V in Hank's solution with different pH values, at 37 °C. I_{corr} is the corrosion current density; E_{corr} is the corrosion potential.

Solutions	I_{corr} ($\mu A \cdot cm^{-2}$)	E_{corr} (V)	Corrosion Rate $\times 10^{-5}$ ($mm \cdot y^{-1}$)
pH 3	0.0964	−0.49006	0.2699
pH 5	0.0632	−0.47519	0.1769
pH 7	0.0334	−0.46669	0.0935

3.3. Potentiostatic Polarization Test

Five different applied potentials (0.6, 0.7, 0.8, 0.9, and 1.0 V_{SCE}) were selected to produce a passive film on the alloy surface in Hank's solution for 2500 s, which are shown in Figure 3. Figure 3a–c exhibits potentiostatic polarization curves of LPBFed Ti–6Al–4V in Hank's solution at various pH values. Each curve begins with a sharp decline and, over time, transforms into a horizontal line. Several relevant types of research have shown that this is the result of the growth of a passive film in the early stage, and the gradual stabilization of the passive film growth in the late stage [22–24]. Generally, the growth and dissolution of the passive film occur simultaneously, so that the later stable passive film should be in a dynamic equilibrium [25,26]. After magnifying the pictures, as shown in the insets of Figure 3, the current transition spikes can be distinguished from the background current. The information regarding these current transition spikes, such as nucleation times, durations, nucleation peaks, and so on, can be seen by continuing the amplification, which has been studied in our previous work [6] and discussed in detail by Burstein et al. [22]. It is known that these current transition spikes can go from nucleation to annihilation in seconds or less, which has been attributed to the self-repair of the passive film. Irreversible, stable pitting corrosion will form if the passive film is not repaired in time. Certainly, more current transition spikes mean a greater tendency toward stable pitting corrosion. For convenience, a statistical analysis was performed, to count the current spikes in PP tests at different potentials in the solutions with different pH values. Therefore, the frequency of pit nucleation was counted and plotted in Figure 4, for a more intuitive comparison of pitting corrosion at different pH values. During the statistics, the first 200 s of data were cut, since, during this time the passive film had not been covered completely, and was unstable on the surface of LPBFed Ti–6Al–4V. The 2500 s duration was averaged into 500 s segments, for a total of 5 segments, and then counted. The frequency of each segment, is

the ratio of the number of current transition spikes in that segment, to the period. It can be seen that the frequency of pit nucleation decreases as the pH increases. In other words, the lower the pH, the more unstable the passive film becomes, and the probability of pitting corrosion increases.

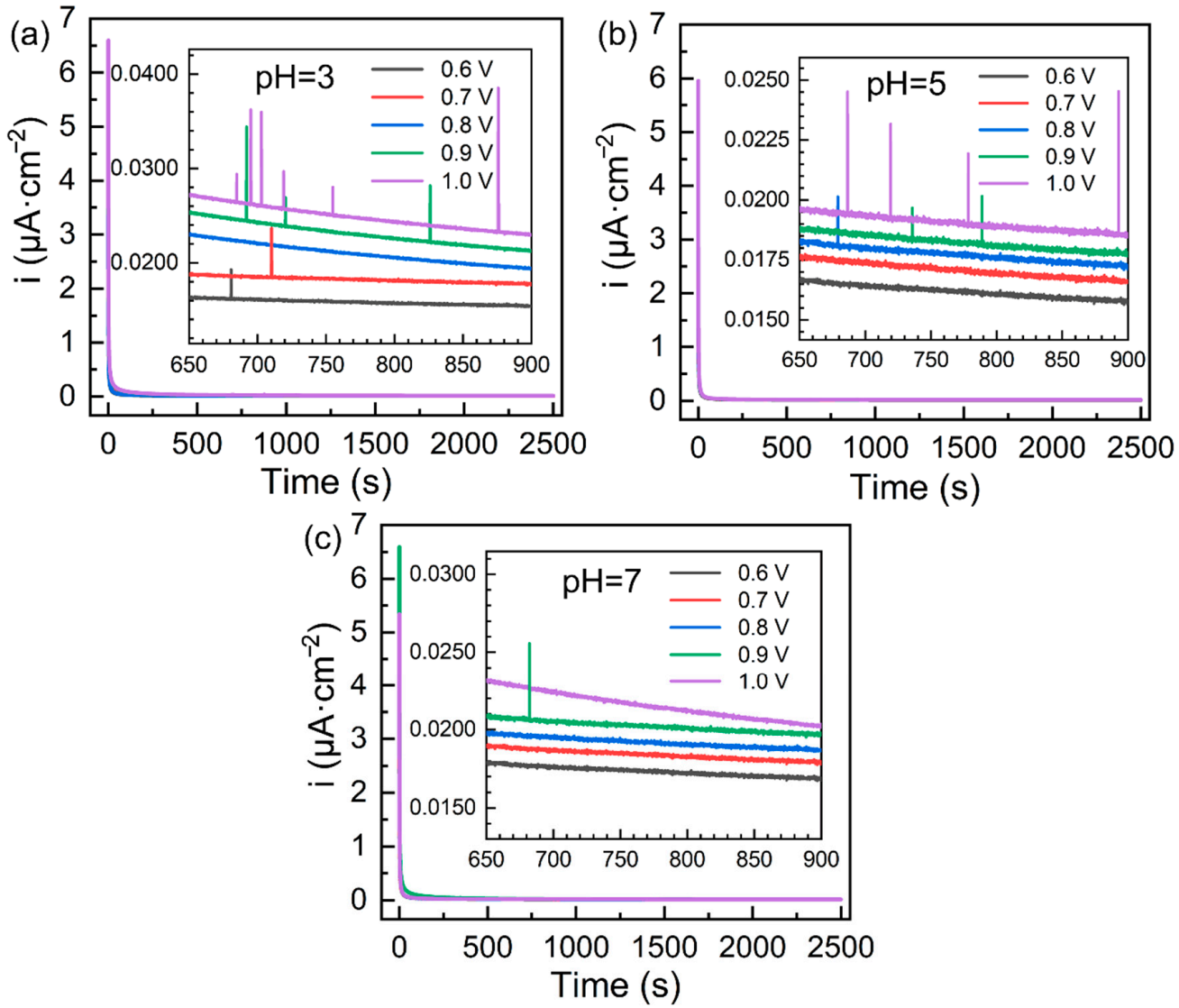

Figure 3. Potentiostatic polarization curves of LPBFed Ti–6Al–4V in Hank's solution at (**a**) pH 3; (**b**) pH 5; and (**c**) pH 7, under 0.6, 0.7, 0.8, 0.9, and 1.0 V_{SCE}. The enlarged regions from 650 to 900 s are shown in the insets.

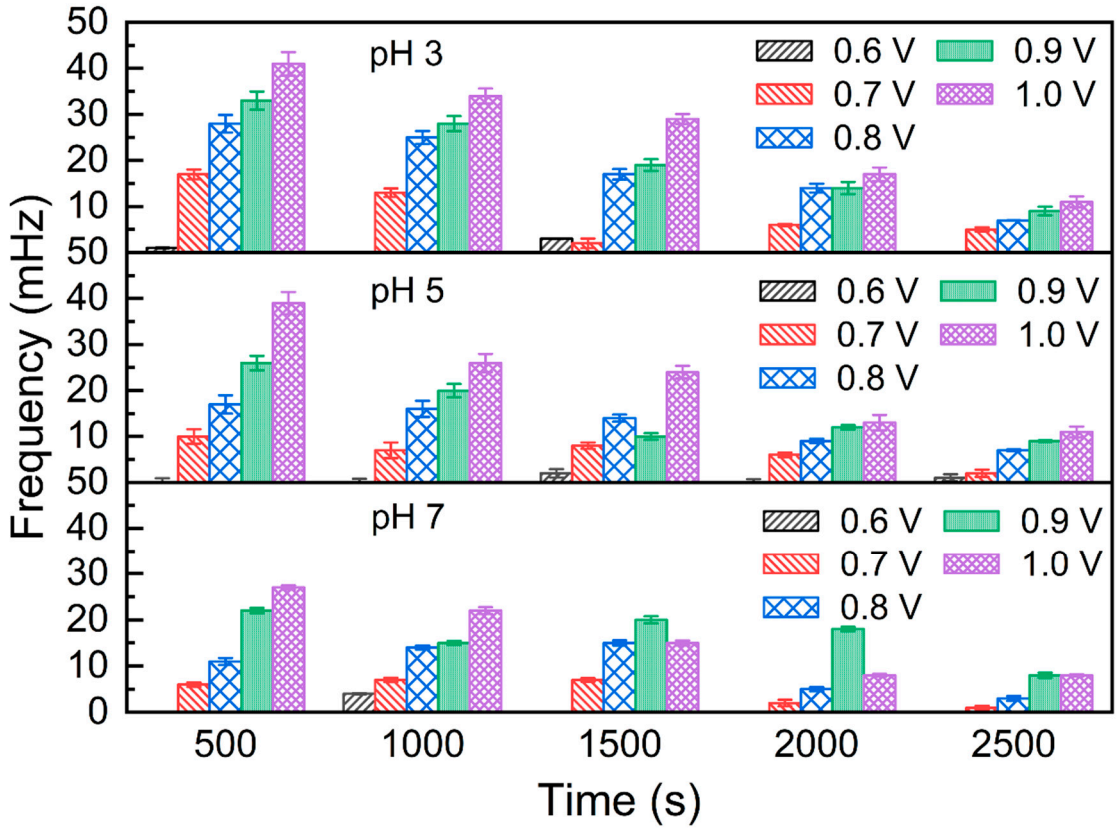

Figure 4. The frequency of pit nucleation for the LPBFed Ti–6Al–4V under the potentials of 0.6, 0.7, 0.8, 0.9, 1.0 V_{SCE}, in Hank's solution (pH = 3, 5, 7) at 37 °C.

3.4. Electrochemical Impedance Spectroscopy after Potentiostatic Polarization

Figure 5 displays the EIS results of LPBFed Ti–6Al–4V in Hank's solution at different pHs after PP. Figure 5a,c,e are Nyquist plots, where a larger radius of the capacitive loop indicates a larger passive film impedance. Therefore, the sample is more resistant in Hank's solution at pH 7, which has the largest capacitive loop compared to those of the other solutions. Figure 5b,d,f are Bode plots, which consist of Bode impendance plots and Bode phase plots. In the high-frequency region (10^3~10^5 Hz) of the Bode phase plots, the phase angle is close to 0°, which demonstrates that the electrolyte resistance is constant. The maximum phase in the mid-frequency region (10^{-1}~10^3 Hz) is approaching 80°, indicating that the sample forms a dense layer on the surface of the solution. Therefore, to clarify the non-capacitive behavior of the passive film formed on the samples, the R(Q(R(QR))) model of the equivalent electrical circuit (EEC) (Figure 5a,c,e insets) was used to fit the EIS data. According to our previous work, the R(Q(R(QR))) model is the most suitable for the ECC fitting of titanium alloys with bilayer properties [6,25,27]. The fitting results are shown in Table 2, where R_s is solution resistance, R_f is passive film resistance, R_{ct} is charge transfer resistance, n is the dispersion index, and CPE is a constant phase element. The value of R_s has an increasing trend, as follows: pH 3 < pH 5 < pH 7. A high solution resistance means poor electrical conductivity. It can be deduced that the electrical conductivity of the solution would be inhibited as the value of pH increases. As a result, the reaction between the solution and the surface of the substrate is slow, and the passive film is thicker, for less dissolution. Unlike the R_s, R_f represents the outer film of LPBFed Ti–6Al–4V, and shows an opposite trend as the value of pH increases. R_{ct} describes the ease of charge transfer from the metal to the solution, and also proved that the sample had preferable corrosion resistance in Hank's solution at pH 7. It is worth noting that R_{ct} represents the dense film inside the passive film. Therefore, the passive film of LPBFed Ti–6Al–4V formed in the solutions at pH 3 is prone to dissolve, which leads to poor corrosion resistance.

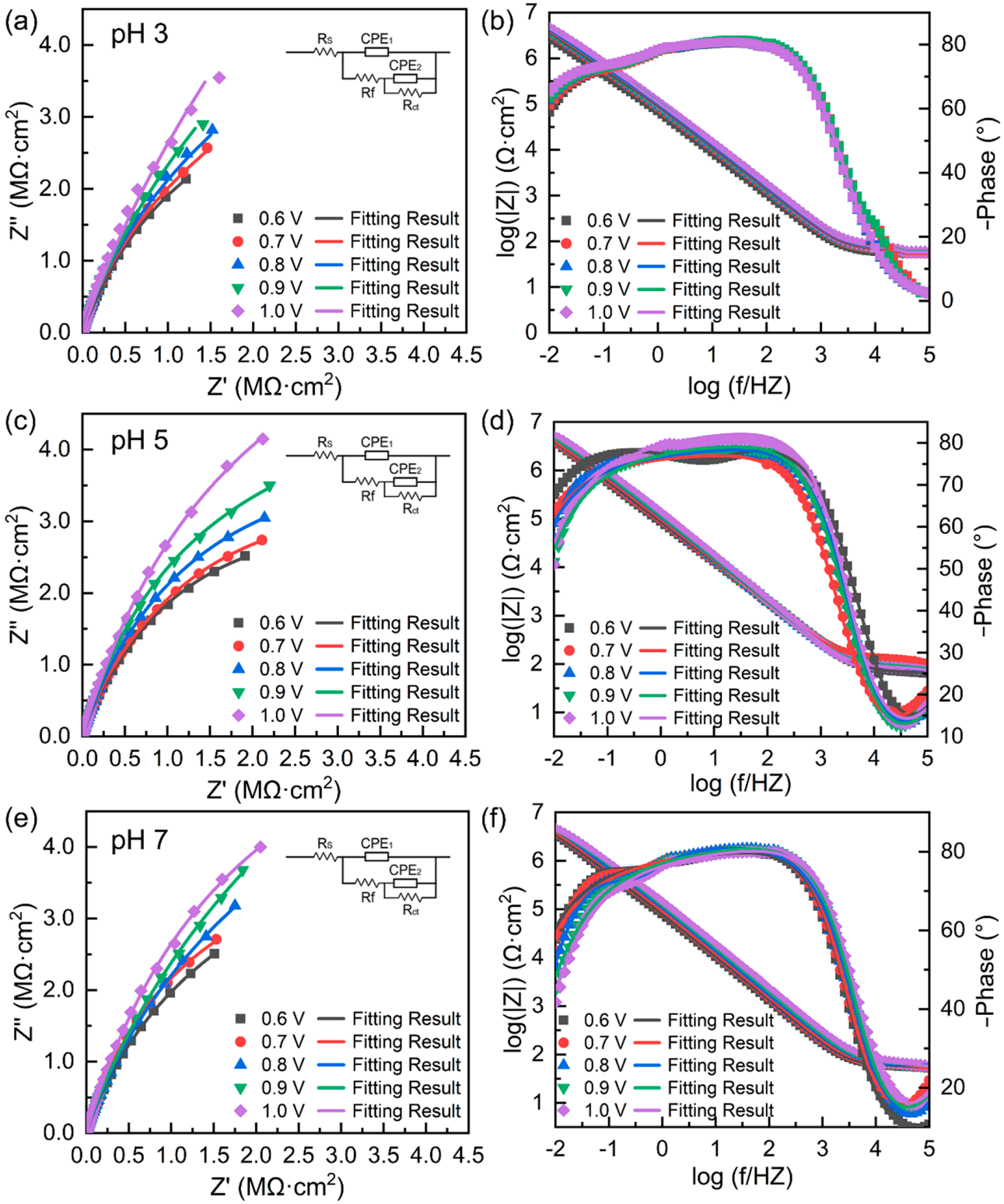

Figure 5. Electrochemical impedance spectroscopy after PP for the LPBFed Ti–6Al–4V, under the potentials of 0.6, 0.7, 0.8, 0.9, 1.0 V_{SCE} in Hank's solution (pH = 3, 5, 7) at 37 °C. (**a**,**c**,**e**) are Nyquist plots; (**b**,**d**,**f**) are Bode plots.

Table 2. Fitting results of EIS from Figure 4. R_s is solution resistance, R_f is passive film resistance, R_{ct} is charge transfer resistance, n is the dispersion index, and CPE is a constant phase element.

Solution	Potential (V_{SCE})	R_s ($\Omega \cdot cm^2$)	$CPE_1 \times 10^{-6}$ ($\Omega^{-1} \cdot s^n \cdot cm^{-2}$)	n_1	R_f ($k\Omega \cdot cm^2$)	$CPE_2 \times 10^{-6}$ ($\Omega^{-1} \cdot s^n \cdot cm^{-2}$)	n_2	R_{ct} ($M\Omega \cdot cm^2$)
pH 3	0.6	11.62 ± 0.54	0.93 ± 0.24	0.91 ± 0.34	13.89 ± 0.10	1.94 ± 0.19	0.93 ± 0.25	6.34 ± 0.14
	0.7	19.26 ± 0.14	0.88 ± 0.07	0.86 ± 0.07	14.40 ± 0.36	1.71 ± 0.09	0.93 ± 0.05	10.14 ± 0.07
	0.8	19.81 ± 0.17	1.15 ± 0.18	0.90 ± 0.33	15.48 ± 0.27	1.56 ± 0.05	0.94 ± 0.13	13.01± 0.04
	0.9	20.42 ± 0.09	1.14 ± 0.22	0.93 ± 0.19	16.33 ± 0.07	1.10 ± 0.04	0.94 ± 0.02	14.37± 0.35
	1.0	18.42 ± 0.03	1.32 ± 0.14	0.95 ± 0.21	19.50 ± 0.06	1.20 ± 0.16	0.97 ± 0.04	16.42 ± 0.34
pH 5	0.6	18.59 ± 0.08	1.08 ± 0.06	0.87 ± 0.12	8.42 ± 0.03	0.89 ± 0.15	0.78 ± 0.09	8.58 ± 0.06
	0.7	18.69 ± 0.14	1.25 ± 0.01	0.97 ± 0.21	9.51 ± 0.21	1.61 ± 0.23	0.89 ± 0.06	15.85 ± 0.07
	0.8	19.11 ± 0.01	0.83 ± 0.13	0.84 ± 0.32	10.96 ± 0.14	1.33 ± 0.11	0.91 ± 0.09	18.46 ± 0.09
	0.9	26.32 ± 0.02	0.73 ± 0.10	0.98 ± 0.04	13.82 ± 0.28	1.18 ± 0.04	0.92 ± 0.06	20.01 ± 0.09
	1.0	24.47 ± 0.22	1.86 ± 0.19	0.89 ± 0.11	17.36 ± 0.07	1.73 ± 0.04	0.94 ± 0.04	21.97 ± 0.07
pH 7	0.6	20.11 ± 0.41	1.02 ± 0.04	0.91 ± 0.29	5.67 ± 0.21	0.93 ± 0.17	0.85 ± 0.26	9.00 ± 0.08
	0.7	24.87 ± 0.02	0.96 ± 0.09	0.97 ± 0.12	6.01 ± 0.11	1.43 ± 0.06	0.94 ± 0.05	16.71 ± 0.02
	0.8	28.42 ± 0.10	1.69 ± 0.06	0.91 ± 0.03	8.88 ± 0.21	1.92 ± 0.15	0.85± 0.09	21.06 ± 0.07
	0.9	30.64 ± 0.17	0.93 ± 0.14	0.96 ± 0.04	10.53 ± 0.04	1.79 ± 0.51	0.95 ± 0.14	23.68 ± 0.06
	1.0	31.46 ± 0.37	1.24 ± 0.30	0.96 ± 0.11	12.05 ± 0.02	1.79 ± 0.08	0.94 ± 0.08	27.03 ± 0.24

3.5. Mott–Schottky Measurements

Figure 6 displays the Mott–Schottky diagrams of LPBFed Ti–6Al–4V in Hank's solution with different pHs, after PP. Generally, Figure 6a–c all exhibit linear regions, with positive slopes between −0.5 and −0.3 V_{SCE}, between −0.6 and −0.4 V_{SCE}, and between −0.7 and −0.5 V_{SCE}, respectively. It can be confirmed that the presence of oxygen vacancies (anion donors) in the passive film represent n-type semiconductive properties. Initially, the thickness of the passive film formed by PP can be measured using the equation below [28]:

$$L_{SS} = \frac{\varepsilon \varepsilon_0 A}{C_{eff}} \quad (2)$$

where ε is the relative dielectric constant of the passive film (TiO_2 is the principal component of the passive film, and equals 60 [28]); ε_0 is the vacuum dielectric constant, and equals 8.85×10^{-14} $F \cdot cm^{-1}$; A is the effective passivation area of Ti electrode (1 cm^2); and C_{eff} is the effective capacitance, which can be derived from the EIS results (at the frequency of 1 kHz, the electrochemical impedance shows an almost purely capacitive behavior [29]) after the potentiostatic polarization test of the passive film. The calculated thickness of the passive film is plotted in Figure 7a, which demonstrates that a low pH of Hank's solution is adverse to the formation of the passive film.

According to the above description, the donor density (N_D, mainly for oxygen vacancies) has a relationship with the slope of the Mott–Schottky curve. Then, N_D can be calculated based on the n-type semiconductive Mott–Schottky expressions: the slope of the curves equals $\frac{2}{\varepsilon \varepsilon_0 e N_D}$ [30], where e is the electron charge (1.6×10^{-19} C). The measured N_D is plotted in Figure 7b, and the relationship between N_D and the applied potential is obtained by fitting the following equation [31]:

$$N_D = \omega_1 e^{-bE} + \omega_2 \quad (3)$$

where ω_1, ω_2, and b are fitting constants in Equation (3), and correspond to the fitted equations in Figure 6b; E is the applied potential. As shown in Figure 6b, N_D decreased with increasing potentials and pH. In addition, the diffusion coefficient of vacancy (D_O) is another important indicator of the passive film, and the growth kinetics of the passive film

also depends on it. The expression for D_O is based on the Nernst–Plank transport equation as follows [32]:

$$D_O = \frac{i_p RT}{4eF\varepsilon_L \omega_2} \quad (4)$$

where i_p is the current density under a stable state, which can be obtained from Figure 3; R is the gas constant (8.314 $J \cdot mol^{-1}$); T is the absolute temperature; F is Faraday's constant (96487 $C \cdot eq^{-1}$); ω_2 can be obtained from Figure 7b. ε_L is the electric field intensity, which has a linear relationship with L_{SS} and E, given by Equation (5) [17]:

$$L_{ss} = \frac{(1-\alpha)E}{\varepsilon_L} + B \quad (5)$$

where α is the surface polarizability and equals 0.5, and B is a constant [33]. As such, ε_L can be determined, and D_O is plotted in Figure 7c. Figure 7c describes the electrochemical reaction at the interface of the passive film/solution. Thus, the growth rate of the passive film formed on LPBFed Ti–6Al–4V in Hank's solution at different pHs can be ordered as follows: pH 7 > pH 5 > pH 3.

Moreover, the kinetics of the film growth can be expressed as Equation (6), based on the point defect model (PDM), expressed as follows [11]:

$$\frac{dL_{SS}}{dt} = J\frac{\Omega}{N_A} \quad (6)$$

where Ω is the molar volume of each cation; t is time; N_A is Avogadro's number; and J is the vacancy flux. According to Fick's first law, J is determined by both the concentration gradient (J_C) and the potential gradient (J_P), listed as follows [34]:

$$J = J_C + J_P \quad (7)$$

The solution was kept in a stable state during the whole test in this work. So, J_C is a constant, while J is heavily impacted by J_P. As a result, the equation may be written as [13]:

$$J_P = q_i K D_0 N_D \quad (8)$$

where q_i is an electric charge and has a value of 2e; and K is defined as $K = \frac{F\varepsilon}{RT}$. As such, q_i and K are considered constants, and the results of J_P are determined by N_D and D_O. Therefore, the calculated J_P is plotted in Figure 7d, which shows that the passive film formed on the LPBFed Ti–6Al–4V in Hank's solution with pH 7, has a high oxygen flux. It indicates that, in the films in which the oxygen vacancies travel quicker, the passive film grows faster, which is consistent with the result that the passive film thickness is thickest at pH 7 (Figure 6a).

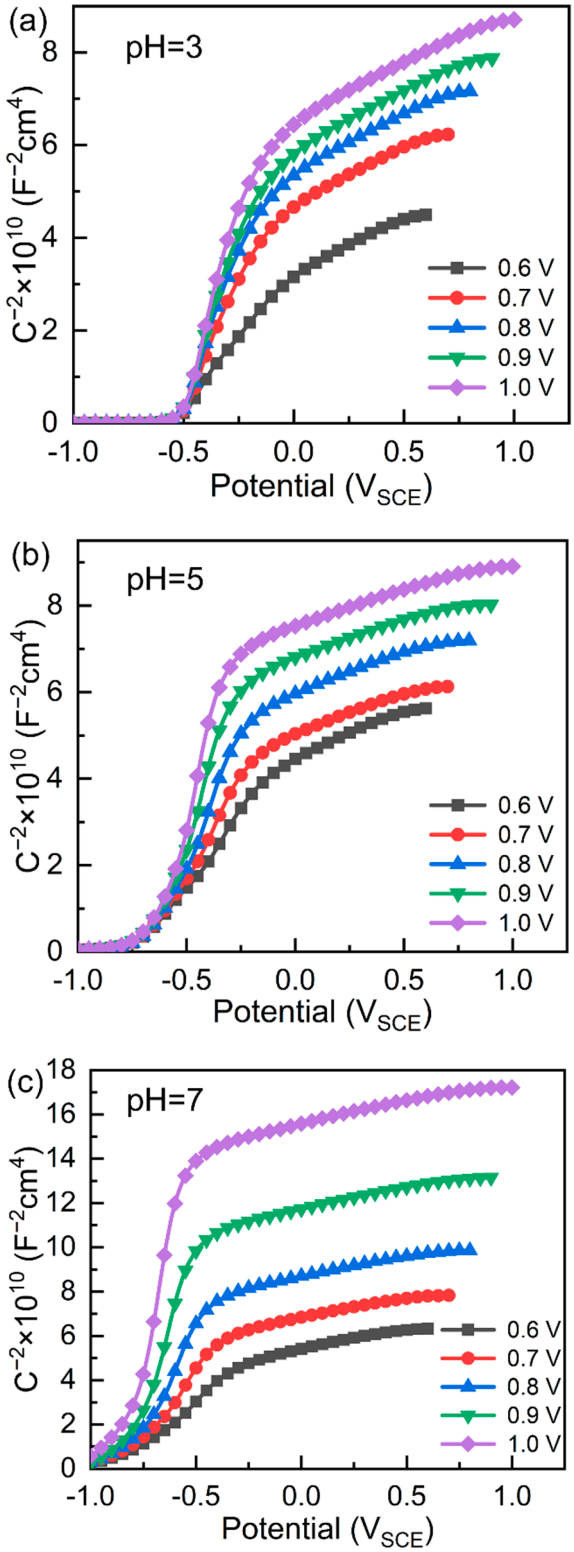

Figure 6. Mott–Schottky curves of potentiostatic polarized LPBFed Ti–6Al–4V in Hank's solution, under the potentials of 0.6, 0.7, 0.8, 0.9, 1.0 V_{SCE}, at (**a**) pH 3, (**b**) pH 5, and (**c**) pH 7.

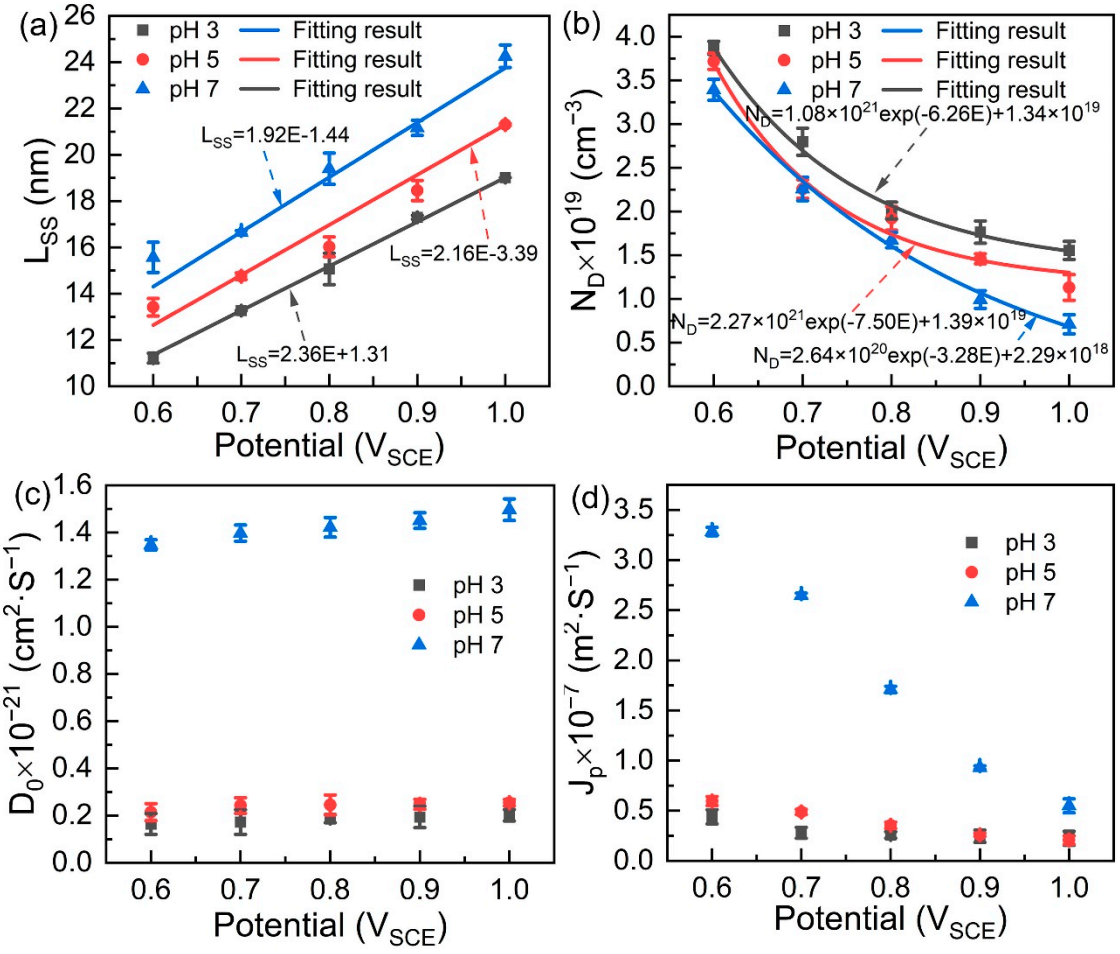

Figure 7. Calculated (**a**) thicknesses (L_{SS}), (**b**) donor densities (N_D), (**c**) vacancy diffusion coefficients (D_O), and (**d**) vacancy fluxes (J_P) of the passive films formed on LPBFed Ti–6Al–4V, under different potentiostatic polarization potentials (0.6, 0.7, 0.8, 0.9 and 1.0 V_{SCE}), in Hank's solution at different pHs.

3.6. XPS Analysis of Passive Films

Figure 8 shows the Ti 2p spectra for LPBFed Ti–6Al–4V, after sputtering at 0 nm, 10 nm, 30 nm, and 60 nm, respectively. It can be noticed that the oxide composition of TiO_2 reaches its maximum at the outmost layer, for all three pH values. The three valences of Ti ions co-exist in the passive film, while their composition varies with pH and sputtering depth. Table 3 lists the composition distribution of Ti ions in each valence state from Figure 8. The content of TiO_2 increases with pH in each depth, while decreasing with the increase in depth. At the surface of the passive film, the fractions of Ti^{4+}, Ti^{3+}, and Ti^{2+} are 85.72 at%, 9.21 at%, and 5.07 at% in Hank's solution at pH 3, respectively. In contrast, the fractions of Ti^{4+}, $Ti^{3+,}$ and Ti^{2+} are 89.67 at%, 5.30 at%, and 5.02 at% in Hank's solution at pH 5, and 89.91 at%, 5.11 at%, and 4.98 at% in Hank's solution at pH 7, respectively. The proportion of Ti^{3+} increased significantly at the sputtering depth of 10 nm. A similar condition is also applied to the fraction of Ti^{2+} at the sputtering depth of 60 nm, of course along with the decline in Ti^{4+}. According to Gebert et al. [35], TiO_2 was produced by the gradual transformation of TiO and Ti_2O_3, so the outmost layer exhibits a passive film dominated by TiO_2. Qin et al. [25] also performed similar research, they found that the aggressive ions (Cl^-) could dissolve the formed TiO_2, and inhibit the transformation of TiO and Ti_2O_3 to TiO_2. Therefore, the transformation process of TiO and Ti_2O_3 to TiO_2 is also applied in this work, and this process could also be suppressed by some ions. Accordingly, the inhibitor in this work is H^+. A lower fraction of suboxides of Ti_2O_3 and TiO could be detected over the

sputtering depths in Hank's solution at pH 7, so a thicker passive film formed, in agreement with the results of Figure 7a.

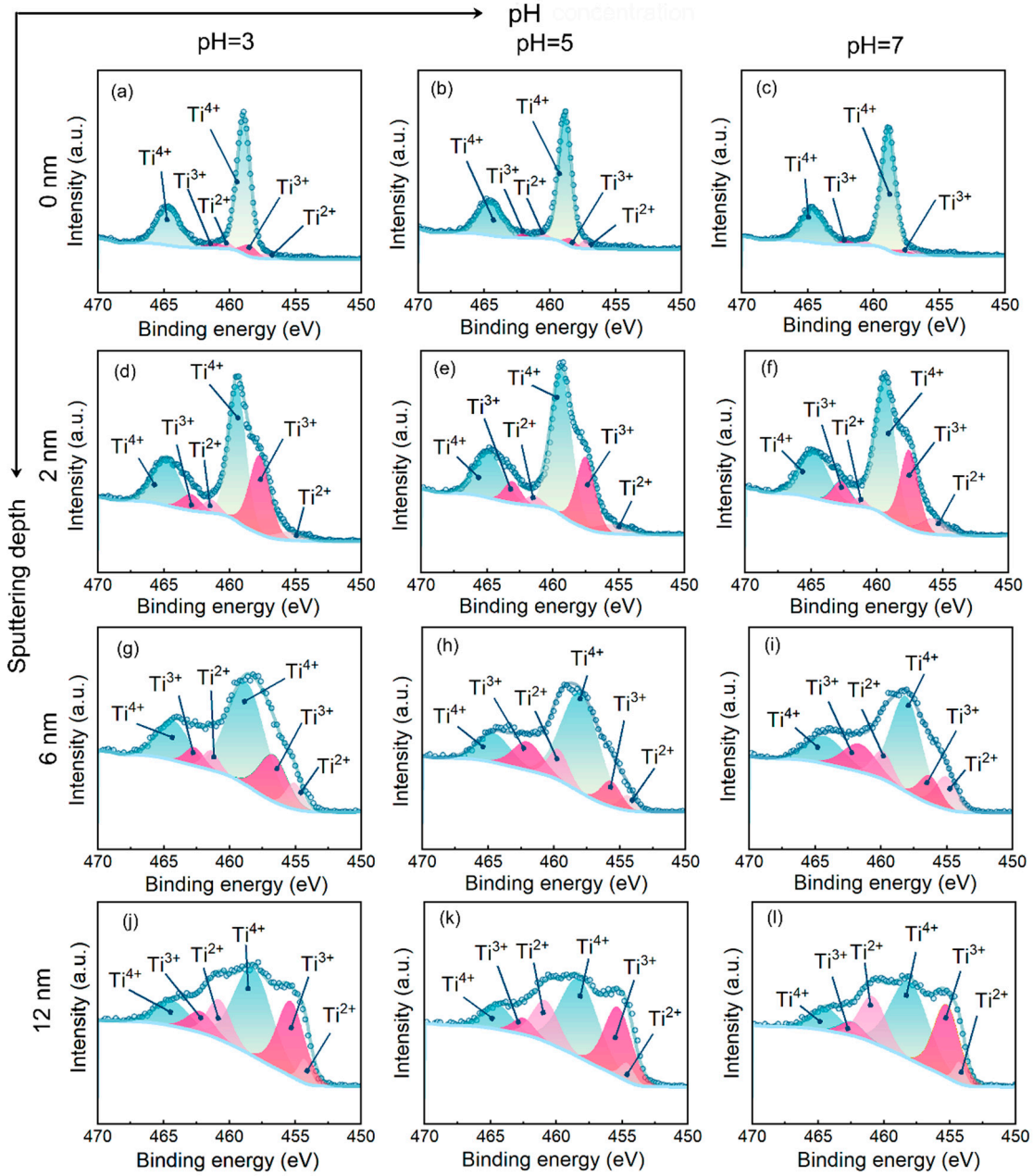

Figure 8. XPS spectrum of Ti 2p region for LPBFed Ti–6Al–4V after 1.0 V_{SCE} PP tests in Hank's solution, with pHs of 3, 5, and 7. Take figure (**a**) as the origin, the figures on the horizontal axis are the result of the solution pH value increases and the figures on the vertical axis is the result of increasing depth of sputtering.

To determine the Cl^- adsorption, XPS spectra of Cl 2p for LPBFed Ti–6Al–4V on the surfaces of the passive film have been conducted, and are shown in Figure 9. The potentiostatic polarization tests, under an applied potential of 1.0 V_{SCE}, were performed, while the peak of Cl^- is obvious for the sample in Hank's solution at pH 3. In addition, the larger the value of pH, the less Cl^- is adsorbed. It can be concluded, that more Cl^- is adsorbed on the surfaces of passive films in Hank's solution with higher H^+ concentration during potentiostatic polarization.

Table 3. Ratios of Ti ions with different valences in the passive films formed on the LPBFed Ti–6Al–4V at different sputtering depths, after potentiostatic polarization under 1.0 V_{SCE} in Hank's solution with different pH values (pH = 3, 5, and 7).

Sputtering Depth (nm)	Solutions	Ti^{4+} (at%)	Ti^{3+} (at%)	Ti^{2+} (at%)
0	pH = 3	85.72	9.21	5.07
	pH = 5	89.67	5.30	5.02
	pH = 7	89.91	5.11	4.98
10	pH = 3	64.23	28.35	7.43
	pH = 5	66.41	26.35	7.24
	pH = 7	68.57	24.55	6.87
30	pH = 3	64.09	23.92	11.98
	pH = 5	68.04	21.67	10.29
	pH = 7	71.86	19.82	8.32
60	pH = 3	52.08	32.66	15.25
	pH = 5	55.35	30.14	14.51
	pH = 7	57.53	28.49	13.98

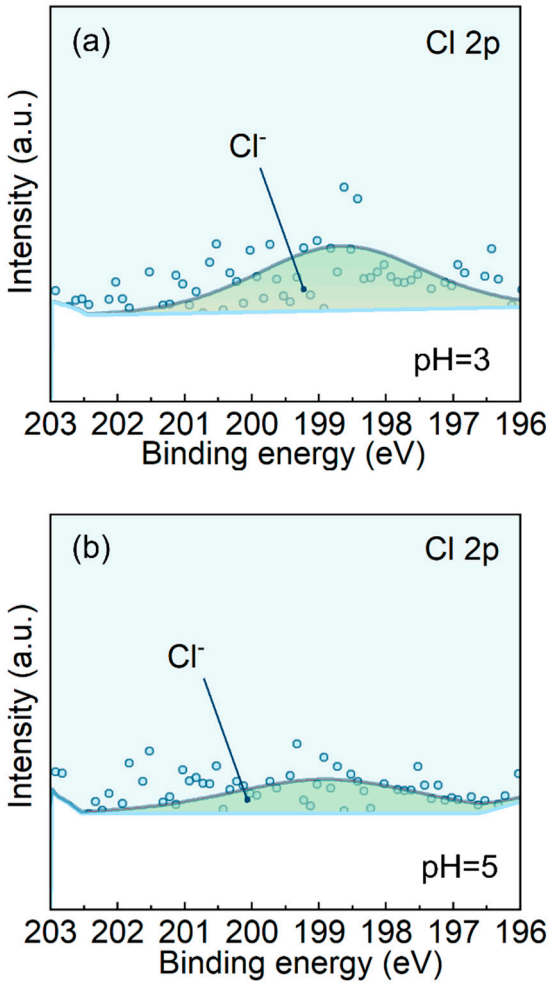

Figure 9. *Cont.*

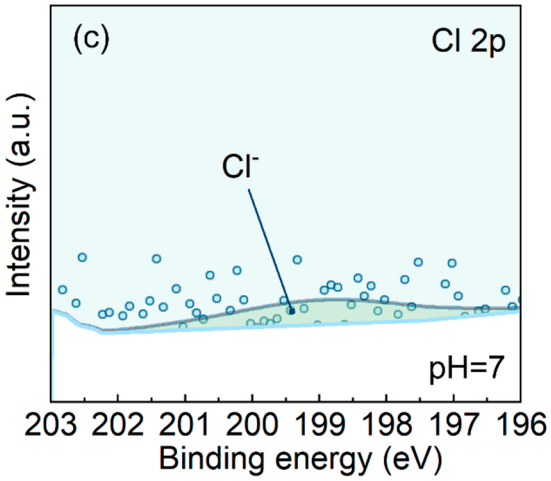

Figure 9. Cl 2p spectra for passive films formed on the surfaces of LPBFed Ti–6Al–4V under 1.0 V_{SCE} in Hank's solution, with pHs of (**a**) 3, (**b**) 5, and (**c**) 7.

4. Discussion

4.1. Effect of H^+ Concentration on the Formed Passive Films

It is widely known that, the greater the concentration of H^+, the smaller the pH value. In this work, the passive films formed on the surface of the LPBFed Ti–6Al–4V in Hank's solution, with different concentrations of H^+, exhibited different properties. Titanium alloy is easy to passivate at room temperature, and the formed passive film (mainly TiO_2) could provide natural protection to avoid corrosion. The oxide layer exhibits good corrosion resistance in aqueous environments and has low electrical conductivity. However, the passive film is sensitive to H^+ in the aqueous environment, and the following hydrolysis reaction occurs between H^+ and the passive film:

$$TiO_2 + 4H^+ \rightarrow 2H_2O + Ti^{4+} \quad (9)$$

Generally, the passive film is always in a dynamic equilibrium of dissolution and generation. The influence of H^+ concentration breaks this equilibrium and accelerates the dissolution. As such, the passive film is thin in Hank's solution with a high H^+ concentration, i.e., low pH, which is in accord with Figure 7a. Furthermore, the composition distribution of Ti^{4+} detected on the surface of the passive film in Hank's solution with high H^+ concentration, is relatively low. It could be speculated that the passive film has undergone a hydrolysis reaction (Reaction (9)) and dissolved, so that a large amount of Ti^{4+} travels into the solution.

In detail, the formation of the passive film is divided into three stages: (i) TiO is the initial form of passivation, it is then quickly oxidized to a trivalent state (Ti_2O_3) by the following reaction:

$$2Ti + 3H_2O - 6e^- \rightarrow Ti_2O_3 + 6H^+ \quad (10)$$

(ii) the new Ti_2O_3 undergoes Reaction (10) and transforms into its tetravalent state ($TiO(OH)_2$) before dehydration:

$$Ti_2O_3 + 4OH^- \rightarrow 2TiO(OH)_2 + H_2O + 4e^- \quad (11)$$

(iii) finally, the stable oxide, TiO_2, is formed via dehydration (Reaction (12)):

$$TiO(OH)_2 \rightarrow TiO_2 + H_2O \quad (12)$$

In this work, the outmost layer of passive film is dominated by TiO_2, according to XPS results, and the suboxides of TiO and Ti_2O_3 are distributed in the internal passive film. It is demonstrated that the formation of the passive film proceeds sequentially from the

inside to the outside with the diffusion of oxygen vacancies. In general, the diffusion rate of oxygen vacancies is faster than cation vacancies, which indicates that a large number of cation vacancies will be left on the surface of the passive film [36,37]. As such, the surface of the passive film presents a negative charge and is prone to absorb H^+. Reaction (9) occurs, and the passive film begins to dissolve. As the concentration of H^+ increases, the reaction intensifies, and the dissolution of the passive film becomes more distinct. That is to say, the passive film becomes reactive due to increased H^+ concentration. It is confirmed again that the thickness of the passive film is thinning with increasing H^+ concentration (Figure 7a). As a consequence, the increase in H^+ concentration inhibits the formation of the passive film and promotes the dissolution of the passive film.

4.2. Effect of H^+ Concentration on the Metastable Pitting Corrosion of LPBFed Ti–6Al–4V

Combined with the above description, H^+ ions aid in the conversion of the passive film from a passive state to an active state, as well as in the adsorption of Cl^- (Figure 9). However, metastable pitting corrosion is the result of the adsorption of Cl^- on the surface of the passive film. Based on the point defect model (PDM), the growth of the passive film depends on the migration of oxygen vacancies, and Cl^- is prone to be trapped by the oxygen ion in the anion site. Figure 10 displays the mechanism of the growth and dissolution of the passive film, defects are expressed by Kröger–Vink notation [38]. Ti_{Ti} is Ti ions in the cation site of the passive film; *Vö* is oxygen vacancies in the passive film; $V_{Ti}^{4\prime}$ is Ti ion vacancies in the passive film; V_{Ti} is vacancies in the Ti substrate; e' is an electron; O_o is an oxygen ion in the anion site of the passive film; $Ti_{(aq)}^{4+}$ is Ti ions in solution [11]. The growth process of the passive film is expressed as Reaction (1) in Figure 10, which indicates that the Ti atom enters into the film and produces *Vö*. Generally, Reaction (9) is the dissolution of the passive film, while Cl^- is introduced by Reaction (2), inFigure 10. This is the result of a high amount of Cl^- being adsorbed on the surface of the passive film in the acidic solution, forcing oxygen atoms to occupy O_o, a process known as competitive adsorption. Guan et al. [31] reported a similar process in acid fluoride-containing solutions. Therefore, the passive film is gradually thinned, by creating soluble chlorides at Cl^--adsorbed locations.

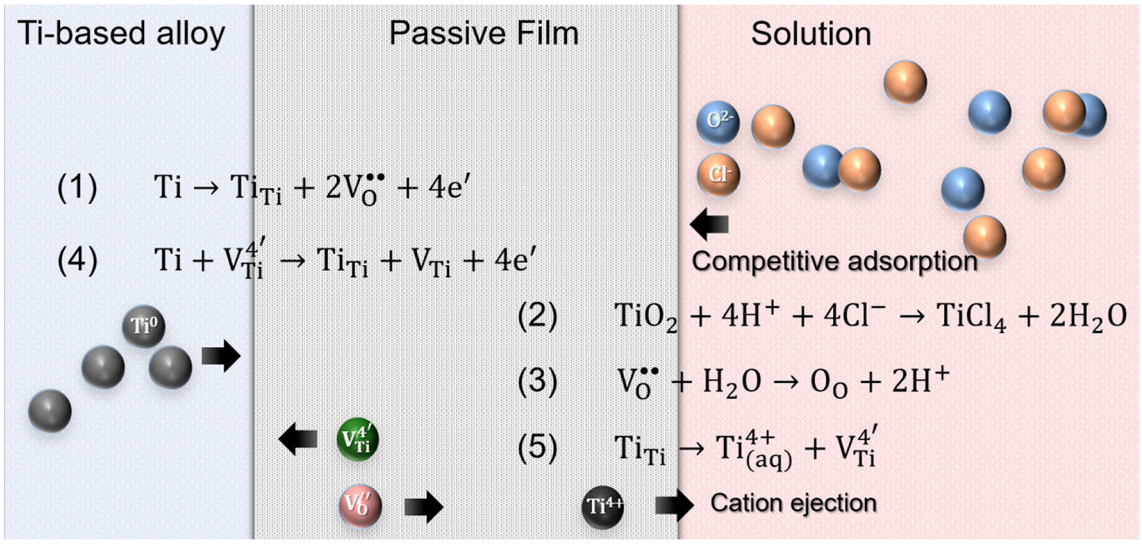

Figure 10. Mechanism of the passive film growth and dissolution according to the point defect model: reactions (1–5) are the physicochemical processes that occur on the passive film. Ti_{Ti} is Ti ions in the cation site of the passive film, *Vö* is oxygen vacancies in the passive film, $V_{Ti}^{4\prime}$ is Ti ion vacancies in the passive film, V_{Ti} is vacancies in the Ti substrate, e' is an electron, O_o is oxygen ion in the anion site of the passive film, $Ti_{(aq)}^{4+}$ is Ti ions in solution.

Furthermore, many researchers proposed three principle mechanisms to simulate a pit that destroys the passive film, and finally erodes the metal substrates, during which the pit nucleates and develops from the passive film [4,39,40]. The three principal mechanisms are: the film-breakdown mechanism, the penetration mechanism, and the adsorption mechanism [1,4,41]. An adsorption mechanism was used in this work, as shown in Figure 11. First of all, as the H^+ concentration increases in Hank's solution, the accumulation of Cl^- on the surface of the passive film also increases (Figure 8). Afterwards, the passive film becomes active and is prone to dissolution. In the meantime, oxygen atoms and chloride ions competitively adsorb in the passive film, as shown in Figure 11. Cl^- is small and aggressive, which squeezes out oxygen atoms, and Cl^- combines with the metal to become soluble chlorides (Reaction (2) in Figure 10). At this moment, macroscopic electrochemistry manifests as current transition spikes and metastable pitting corrosion can be observed, which is demonstrated in Figure 3. The thickness of the passive film is thinned in this way, as shown in Figure 11. In addition, the passive film itself tends to dissolve in an acidic environment.

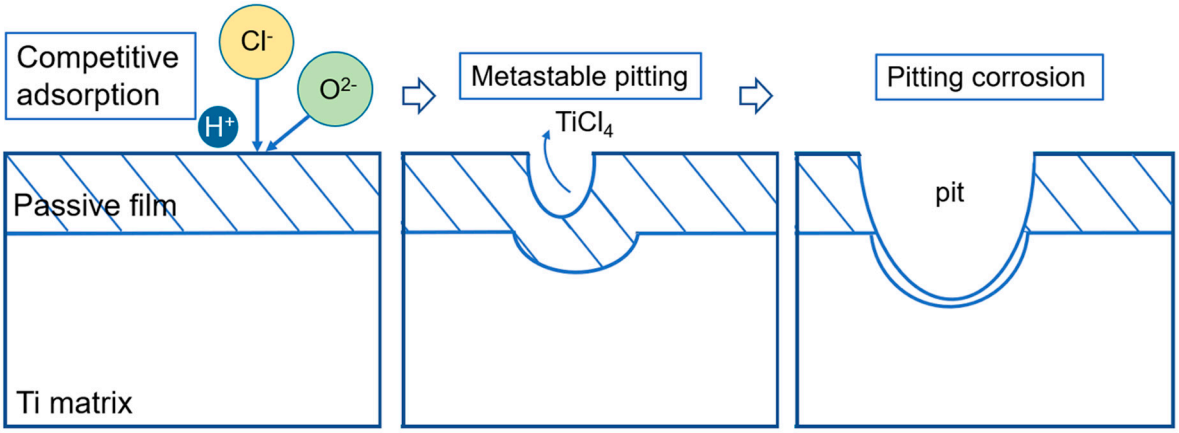

Figure 11. Diagram of the adsorption mechanism of the passive film in acidic solution.

5. Conclusions

In this work, the metastable pitting corrosion behavior of laser powder bed fusion (LPBF)-produced Ti–6Al–4V, in Hank's solutions, at different pH (3, 5, and 7) has been investigated. Meanwhile, the properties of passive films formed in an acidic environment were also researched. The principle conclusions are summarized below:

(1) In the polarization tests, the LPBFed Ti–6Al–4V, in Hank's solutions, at different pH (3, 5, and 7) shows metastable pitting corrosion. With the increase in H^+ concentration, the frequency of metastable pitting corrosion becomes greater, and the possibility of pitting corrosion is also higher.

(2) The passive film formed on the LPBFed Ti–6Al–4V mainly contains TiO_2, based on XPS results, while the content decreases with increasing H^+ concentration. Coupled with Motty–Schottky tests, the transformation process of TiO_2 from TiO and Ti_2O_3 was suppressed by H^+. As such, the passive film has a thin thickness in Hank's solution at pH 3.

(3) The surface of the passive film becomes active in an acidic solution and is prone to dissolve. Meanwhile, more Cl^- were attracted to the surface of the passive film. There was competitive adsorption of Cl^- and oxygen atoms on the passive film, resulting in soluble chlorides. According to the adsorption mechanism, the metastable pitting corrosion would form at the Cl^- adsorption sites.

Author Contributions: Conceptualization: Y.C., L.C., L.W., J.C. and L.Z.; writing—original draft preparation: Y.C.; writing—review and editing: L.C., L.W., J.C. and L.Z.; writing—manuscript

finalization: L.C. and L.Z.; supervision: L.C. and L.Z.; project administration: L.C. and L.Z.; funding acquisition: L.C. and L.Z. All authors have read and agreed to the published version of the manuscript.

Funding: The authors would like to acknowledge the financial support provided by the Jiangsu Province six talent peaks project (XCL-117), the Australian Research Council Discovery Project (DP110101653), the Open Foundation of Guangxi Key Laboratory of Processing for Non-ferrous Metals and Featured Materials, Guangxi University (Grant No. 2020GXYSOF01, 2019GXYSOF01), and the Key Research and Development Program of Shaanxi (Program No.2020GY-251).

Acknowledgments: The authors are grateful to Liqiang Wang and Qin Peng.

Conflicts of Interest: The authors declare no conflict of interest.

References

1. Cui, Y.-W.; Chen, L.-Y.; Liu, X.-X. Pitting corrosion of biomedical titanium and titanium alloys: A brief review. *Curr. Nanosci.* **2021**, *17*, 241–256. [CrossRef]
2. Chen, L.-Y.; Cui, Y.-W.; Zhang, L.-C. Recent development in beta titanium alloys for biomedical applications. *Metals* **2020**, *10*, 1139. [CrossRef]
3. Loto, R.T. Pitting corrosion evaluation and inhibition of stainless steels: A review. *J. Mater. Environ. Sci.* **2015**, *6*, 2750–2762.
4. Frankel, G.S. Pitting Corrosion of Metals: A Review of the Critical Factors. *J. Electrochem. Soc.* **1998**, *145*, 2186–2198. [CrossRef]
5. Chelariu, R.; Bolat, G.; Izquierdo, J.; Mareci, D.; Gordin, D.M.; Gloriant, T.; Souto, R.M. Metastable beta Ti-Nb-Mo alloys with improved corrosion resistance in saline solution. *Electrochim. Acta* **2014**, *137*, 280–289. [CrossRef]
6. Cui, Y.-W.; Chen, L.-Y.; Qin, P.; Li, R.; Zang, Q.; Peng, J.; Zhang, L.; Lu, S.; Wang, L.; Zhang, L.-C. Metastable pitting corrosion behavior of laser powder bed fusion produced Ti-6Al-4V in Hank's solution. *Corros. Sci.* **2022**, *203*, 110333. [CrossRef]
7. Tian, W.; Du, N.; Li, S.; Chen, S.; Wu, Q. Metastable pitting corrosion of 304 stainless steel in 3.5% NaCl solution. *Corros. Sci.* **2014**, *85*, 372–379. [CrossRef]
8. Basame, S.B.; White, H.S. Pitting corrosion of titanium the relationship between pitting potential and competitive anion adsorption at the oxide film/electrolyte interface. *J. Electrochem. Soc.* **2000**, *147*, 1376. [CrossRef]
9. Garfias-Mesias, L.F.; Alodan, M.; James, P.I.; Smyri, W.H. Determination of precursor sites for pitting corrosion of polycrystalline titanium by using different techniques. *J. Electrochem. Soc.* **1998**, *145*, 2005. [CrossRef]
10. Casillas, N.; Charlebois, S.; Smyrl, W.H.; White, H.S. Pitting corrosion of titanium. *J. Electrochem. Soc.* **1994**, *141*, 636. [CrossRef]
11. Macdonald, D.D. The history of the Point Defect Model for the passive state: A brief review of film growth aspects. *Electrochim. Acta* **2011**, *56*, 1761–1772. [CrossRef]
12. Seo, D.-I.; Lee, J.-B. Corrosion Characteristics of Additive-Manufactured Ti-6Al-4V Using Microdroplet Cell and Critical Pitting Temperature Techniques. *J. Electrochem. Soc.* **2019**, *166*, C428–C433. [CrossRef]
13. Seo, D.-I.; Lee, J.-B. Effects of competitive anion adsorption (Br− or Cl−) and semiconducting properties of the passive films on the corrosion behavior of the additively manufactured Ti–6Al–4V alloys. *Corros. Sci.* **2020**, *173*, 108789. [CrossRef]
14. Jaquez-Muñoz, J.; Gaona-Tiburcio, C.; Lira-Martinez, A.; Zambrano-Robledo, P.; Maldonado-Bandala, E.; Samaniego-Gamez, O.; Nieves-Mendoza, D.; Olguin-Coca, J.; Estupiñan-Lopez, F.; Almeraya-Calderon, F. Susceptibility to Pitting Corrosion of Ti-CP2, Ti-6Al-2Sn-4Zr-2Mo, and Ti-6Al-4V Alloys for Aeronautical Applications. *Metals* **2021**, *11*, 1002. [CrossRef]
15. Qu, Q.; Wang, L.; Chen, Y.; Li, L.; He, Y.; Ding, Z. Corrosion behavior of titanium in artificial saliva by lactic acid. *Materials* **2014**, *7*, 5528–5542. [CrossRef]
16. Chen, L.-Y.; Liang, S.-X.; Liu, Y.; Zhang, L.-C. Additive manufacturing of metallic lattice structures: Unconstrained design, accurate fabrication, fascinated performances, and challenges. *Mater. Sci. Eng. R Rep.* **2021**, *146*, 100648. [CrossRef]
17. Chen, L.-Y.; Zhang, H.-Y.; Zheng, C.; Yang, H.-Y.; Qin, P.; Zhao, C.; Lu, S.; Liang, S.-X.; Chai, L.; Zhang, L.-C. Corrosion behavior and characteristics of passive films of laser powder bed fusion produced Ti–6Al–4V in dynamic Hank's solution. *Mater. Des.* **2021**, *208*, 109907. [CrossRef]
18. Zhang, L.C.; Chen, L.Y. A review on biomedical titanium alloys: Recent progress and prospect. *Adv. Eng. Mater.* **2019**, *21*, 1801215. [CrossRef]
19. Zhang, L.C.; Kim, K.B.; Yu, P.; Zhang, W.Y.; Kunz, U.; Eckert, J. Amorphization in mechanically alloyed (Ti, Zr, Nb)–(Cu, Ni)–Al equiatomic alloys. *J. Alloy. Compd.* **2007**, *428*, 157–163. [CrossRef]
20. Zhang, L.C.; Xu, J.; Ma, E. Consolidation and properties of ball-milled $Ti_{50}Cu_{18}Ni_{22}Al_4Sn_6$ glassy alloy by equal channel angular extrusion. *Mater. Sci. Eng. A* **2006**, *434*, 280–288. [CrossRef]
21. Zhang, L.C.; Xu, J.; Ma, E. Mechanically alloyed amorphous $Ti_{50}(Cu_{0.45}Ni_{0.55})_{44-x}Al_xSi_4B_2$ alloys with supercooled liquid region. *J. Mater. Res.* **2002**, *17*, 1743–1749. [CrossRef]
22. Burstein, G.T.; Liu, C.; Souto, R.M. The effect of temperature on the nucleation of corrosion pits on titanium in Ringer's physiological solution. *Biomaterials* **2005**, *26*, 245–256. [CrossRef] [PubMed]
23. Escrivà-Cerdán, C.; Blasco-Tamarit, E.; García-García, D.M.; García-Antón, J.; Akid, R.; Walton, J. Effect of temperature on passive film formation of UNS N08031 Cr–Ni alloy in phosphoric acid contaminated with different aggressive anions. *Electrochim. Acta* **2013**, *111*, 552–561. [CrossRef]

24. Kong, D.; Dong, C.; Zhao, M.; Ni, X.; Man, C.; Li, X. Effect of chloride concentration on passive film properties on copper. *Corros. Eng. Sci. Technol.* **2018**, *53*, 122–130. [CrossRef]
25. Qin, P.; Chen, L.Y.; Liu, Y.J.; Jia, Z.; Liang, S.X.; Zhao, C.H.; Sun, H.; Zhang, L.C. Corrosion and passivation behavior of laser powder bed fusion produced Ti-6Al-4V in static/dynamic NaCl solutions with different concentrations. *Corros. Sci.* **2021**, *191*, 109728. [CrossRef]
26. Munirathinam, B.; Narayanan, R.; Neelakantan, L. Electrochemical and semiconducting properties of thin passive film formed on titanium in chloride medium at various pH conditions. *Thin Solid Film.* **2016**, *598*, 260–270. [CrossRef]
27. Cui, Y.-W.; Chen, L.-Y.; Chu, Y.-H.; Zhang, L.; Li, R.; Lu, S.; Wang, L.; Zhang, L.-C. Metastable pitting corrosion behavior and characteristics of passive film of laser powder bed fusion produced Ti–6Al–4V in NaCl solutions with different concentrations. *Corros. Sci.* **2023**, *215*, 111017. [CrossRef]
28. Gai, X.; Bai, Y.; Li, J.; Li, S.; Hou, W.; Hao, Y.; Zhang, X.; Yang, R.; Misra, R.D.K. Electrochemical behaviour of passive film formed on the surface of Ti-6Al-4V alloys fabricated by electron beam melting. *Corros. Sci.* **2018**, *145*, 80–89. [CrossRef]
29. Sun, F.; Meng, G.; Zhang, T.; Shao, Y.; Wang, F.; Dong, C.; Li, X. Electrochemical corrosion behavior of nickel coating with high density nano-scale twins (NT) in solution with Cl^-. *Electrochim. Acta* **2009**, *54*, 1578–1583. [CrossRef]
30. Duan, Z.; Man, C.; Dong, C.; Cui, Z.; Kong, D.; Wang, X. Pitting behavior of SLM 316L stainless steel exposed to chloride environments with different aggressiveness: Pitting mechanism induced by gas pores. *Corros. Sci.* **2020**, *167*, 108520. [CrossRef]
31. Guan, L.; Li, Y.; Wang, G.; Zhang, Y.; Zhang, L.-C. pH dependent passivation behavior of niobium in acid fluoride-containing solutions. *Electrochim. Acta* **2018**, *285*, 172–184. [CrossRef]
32. Wang, L.; Yu, H.; Wang, S.; Chen, B.; Wang, Y.; Fan, W.; Sun, D. Quantitative analysis of local fine structure on diffusion of point defects in passive film on Ti. *Electrochim. Acta* **2019**, *314*, 161–172. [CrossRef]
33. Chen, Y.; Zhang, J.; Gu, X.; Dai, N.; Qin, P.; Zhang, L.-C. Distinction of corrosion resistance of selective laser melted Al-12Si alloy on different planes. *J. Alloy. Compd.* **2018**, *747*, 648–658. [CrossRef]
34. Guo, H.X.; Lu, B.T.; Luo, J.L. Study on passivation and erosion-enhanced corrosion resistance by Mott-Schottky analysis. *Electrochim. Acta* **2006**, *52*, 1108–1116. [CrossRef]
35. Gebert, A.; Oswald, S.; Helth, A.; Voss, A.; Gostin, P.F.; Rohnke, M.; Janek, J.; Calin, M.; Eckert, J. Effect of indium (In) on corrosion and passivity of a beta-type Ti–Nb alloy in Ringer's solution. *Appl. Surf. Sci.* **2015**, *335*, 213–222. [CrossRef]
36. Bojinov, M. The ability of a surface charge approach to describe barrier film growth on tungsten in acidic solutions. *Electrochim. Acta* **1997**, *42*, 3489–3498. [CrossRef]
37. Bojinov, M. Modelling the formation and growth of anodic passive films on metals in concentrated acid solutions. *J. Solid State Electrochem.* **1997**, *1*, 161–171. [CrossRef]
38. Dong, Y.; Qi, L.; Li, J.; Chen, I.W. A computational study of yttria-stabilized zirconia: II. Cation diffusion. *Acta Mater.* **2017**, *126*, 438–450. [CrossRef]
39. Brenna, A.; Ormellese, M.; Lazzari, L. Electromechanical breakdown mechanism of passive film in alternating current-related corrosion of carbon steel under cathodic protection condition. *Corrosion* **2016**, *72*, 1055–1063.
40. Al Saadi, S.; Yi, Y.; Cho, P.; Jang, C.; Beeley, P. Passivity breakdown of 316L stainless steel during potentiodynamic polarization in NaCl solution. *Corros. Sci.* **2016**, *111*, 720–727. [CrossRef]
41. Zhang, B.; Wang, J.; Wu, B.; Guo, X.W.; Wang, Y.J.; Chen, D.; Zhang, Y.C.; Du, K.; Oguzie, E.E.; Ma, X.L. Unmasking chloride attack on the passive film of metals. *Nat. Commun.* **2018**, *9*, 2559. [CrossRef] [PubMed]